https://doi.org/10.26599/FRICT.2026.9441261

Research Article

Selenium-doped WS_2 for humid-air lubricity via weakened interfacial hydrogen bonding

Yuqian Huang [a,b] [1], Bin Zhang [a] [1], Zhiwei wang [b], Zaixiu Yang [a*], Zhenwei Niu [b], Kaixiong Gao [a], Junyan Zhang [a], Goksel Hizli [c], Kürşat Kazmanlı [c], Ahmet T. Alpas [d]

a State Key Laboratory of Solid Lubrication, Lanzhou Institute of Chemical Physics, Chinese Academy of Science, Lanzhou 730000, China
b School of National Defense Science & Technology, Southwest University of Science and Technology, Mianyang 621010, China
c Department of Metallurgical and Materials Engineering, Istanbul Technical University, Istanbul 34469, Turkey
d Tribology of Materials Research Centre, Department of Mechanical, Automotive & Materials Engineering, University of Windsor, Windsor, ON N9B 3P4, Canada

* Zaixiu Yang: yangzaixiu@licp.cas.cn

Received: October 17, 2025; Revised: March 9, 2026; Accepted: May 7, 2026

Abstract:

The degradation of WS_2's tribological performance in humid environments represents a persistent scientific and practical challenge, limiting its application scope despite its excellent lubricity in inert atmospheres. While the superior moisture tolerance of WSe_2 has been recognized, the fundamental atomic-scale mechanisms governing this difference remain inadequately understood. This work addresses this critical knowledge gap by revealing that the disparity originates from the distinct hydrogen bond strengths formed at the material-water interface. Through integrated density functional theory (DFT) calculations and experimental validation, we quantitatively demonstrate that

[1] These two authors contributed equally: Yuqian Huang and Bin Zhang

water molecules form significantly weaker O–H···Se hydrogen bonds with WSe_2 (bond lengths: 3.02–3.25 Å) compared to O–H···S bonds with WS_2 (2.80–2.98 Å). This fundamental difference manifests functionally as a 35% lower interlayer sliding energy barrier for WSe_2 under humid conditions, providing the first atomistic explanation for its sustained lubricity. Leveraging this mechanistic insight, we propose and validate a novel materials design strategy: selectively doping selenium into the WS_2 lattice to engineer its interfacial chemistry. The developed W-S-Se coating exhibits remarkable performance, achieving an 18% reduction in coefficient of friction and a 78% decrease in wear rate at 40% RH compared to pristine WS_2. Extensive characterization confirms the formation of a re-oriented, crystalline transfer layer with insignificant oxidation. This study establishes a new paradigm for solid lubricant design, shifting the focus from conventional microstructure optimization towards direct atomic-level engineering of interfacial water interactions, opening avenues for developing advanced lubricants operable across diverse environmental conditions.

KEYWORDS: WS_2, Selenium doping, Friction, Moisture, Hydrogen bonds, DFT

1. Introduction

Transition metal dichalcogenides (TMD) are layered materials with each sandwich-like layer consisting of transition metal atoms (Mo, W) covalently bond to chalcogen atoms (S, Se, Te) [1]. The layers are stacked through van der Waals interactions, resulting in low interlayer adhesion. This interlayer structure allows for easy shearing of the TMD layers and exhibits low/super-low coefficients of friction (COF) in vacuum and dry environments [2]. Hence, WS_2 and MoS_2 are the most widely used TMDs as solid lubricants in the nuclear [3, 4] and aerospace [5, 6] industries where they mitigate friction and wear in sliding components such as bearings and gears. However, both materials suffer from a long-standing challenge of substantial deterioration of tribological performance when exposed to humid environments [7-9]. For instance, Prasad et al. [8] found that the coefficient of friction (COF) of WS_2 increased from 0.04 in dry nitrogen to 0.10-0.15 in air with 60% relative humidity (RH). Since exposure of the WS_2 and MoS_2 films to humid environments is inevitable during storage and testing, establishing viable strategies for designing TMDs films resistant to moisture-induced degradation remains an urgent task.

Understanding the friction mechanisms of TMD films in humid environments is essential for developing films for harsh conditions. While early studies indicated that H_2O molecules induce oxidation to form MoO_3 and WO_3 [10-12], recent evidence suggests that physisorbed water and the resulting interfacial hydrogen bonds play a more critical role. For instance, oxidation during the sliding process only occurs to a limited extent. In contrast, AFM tests without oxide formation [13] showed increased friction of MoS_2 in a humid environment. Bondarev et al. [14] further illustrated that oxygen content does not necessarily degrade the tribological performance of MoS_2. Similarly, introducing WO_3 into WS_2 resulted in a lower COF and a longer wear life than those of WS_2 [15]. Furthermore, the presence of oxides does not necessarily increase friction, as the oxides would form incommensurate contacts with MoS_2 and WS_2 which may lead to superlubricity [14-18].

Recent studies indicated that H_2O physically adsorbs at the interface of MoS_2 and WS_2 may impede layer shearing and increase friction [19-21]. Khare et al. [20] found

that the COF of MoS_2 increases with moisture at temperatures below 100°C, regardless of the presence of oxygen. The friction recovery observed by alternating the testing atmospheres between humid air and dry N_2 further excludes the oxidation process dominating friction, as the oxidation process is likely rate-limited and occurs at limited extent due to energy barriers associated with removing S from the planes [21]. Compared to oxidation that requires overcoming certain energy barriers, physisorption of H_2O on MoS_2 and WS_2 is thermodynamically more feasible due to the release of adsorption energy. Li et al. found that water molecules can form water clusters at the interfaces of TMDs [22]. Bobbitt et al. found that water tends to adsorb on defects in MoS_2, leading to adverse effects on friction [23]. Using sliding friction experiments coupled with density functional theory (DFT) computations, the authors discovered that H_2O physisorption was promoted by the presence of defects and may eventually lead to dissociative adsorption of the molecules, which would serve as initial stage of oxidation [21, 24, 25]. However, it was found the dissociated H_2O would not affect layer adhesion, whereas undissociated H_2O would form O-H···S-type interfacial hydrogen bonds that increase layer adhesion and impede layer sliding, thereby increasing friction.

Besides the popular strategies for improving the tribological properties of WS_2 and MoS_2 in humid environments by enhancing mechanical strength or antioxidant properties [26-29], performance can also be improved by inhibiting the formation of hydrogen bonds. Sun et al. [30] achieved superlubricity of MoS_2 under 30% RH through the in-situ formation of a $MoS_2/S_8/MoS_2$ interface, which suppressed interfacial hydrogen bond formation by layer expansion. Notably, WSe_2 and $MoSe_2$ retain excellent tribological performance under humid conditions, despite sharing the same crystal structure as MoS_2 and WS_2 [31, 32]. Selenide materials demonstrate favorable lubricating performance under humid conditions [33-39] and tellurides also exhibit better potential friction performance [40]. However, the origin of the disparities in tribological behavior between selenides and sulfides under humid conditions is still unclear, necessitating further in-depth study. We hypothesize that the superior

performance of WSe_2 stems from inherently weaker interfacial hydrogen bonding (O–H···Se) compared to that in WS_2 (O–H···S).

Herein, we investigate this hypothesis and leverage it as a materials design principle. We first employ DFT to quantify the hydrogen bond strength, interlayer adhesion, and sliding energy barriers for WS_2 and WSe_2 in the presence of water. Guided by the computational prediction that Se weakens water-layer interactions, we then demonstrate the efficacy of Se doping in dramatically enhancing the humidity tolerance of WS_2 coatings. The advanced nature of this study is demonstrating that the friction performance in humid environments of WS_2 could be dictated by modulating interfacial hydrogen bonds, thereby providing new insights for designing solid lubricants.

2. Materials and methods

2.1 Film preparation

Three films of WS_2, WSe_2 and Se-doped W-S-Se were deposited on Si wafers by high power impulse magnetron sputtering (HIPIMS) technique. The WS_2 and WSe_2 films were deposited using WS_2 and WSe_2 targets with 99.99 wt.% purity while the W-S-Se films were deposited using a homemade WS_2/WSe_2 (mole ratio 3:1) composite target. The composite target enables uniform and stable Se incorporation during deposition, simplifies the fabrication process, improves film compositional homogeneity. Before the deposition process, the vacuum chamber was evacuated to a pressure of 5.0×10^{-3} Pa, and argon gas was introduced into the chamber at a flow rate of 50 sccm maintaining the chamber pressure at 1.1 Pa. The silicon wafers were cleaned by argon ion bombardment at a bias voltage of 600 V for 15 minutes to remove the surface oxide layer. To improve the adhesion to the Si substrate, a Ti transition layer was deposited by medium frequency magnetron sputtering system at a current of 0.5 A and a bias voltage of 50 V for 10min. The WS_2, WSe_2, and W-S-Se films were deposited using sputtering power of 3 KW, voltage 720 V, current 3 A, and bias voltage 50 V,

with a sputtering time of 120 minutes. The compositions of the prepared films obtained from the EDS results are shown in Table 1.

Table 1. Compositions for the pure WS_2 film, WSe_2 films and the W-S-Se film.

Sample	W (at%)	S (at%)	Se (at%)
WS_2	43.7	56.3	0
WSe_2	42.2	0	57.8
W-S-Se	42.1	28.9	29.0

2.2 Tribological test

Tribological tests were conducted using a ball-on-disk tribometer (CSM TRB3, Anton Paar) in room temperature (25 ℃). In order to investigate the effect of humidity on the friction of the films, friction tests were carried out in dry air, and air with 25% and 40% RH. Humidity is controlled by introducing dry gas into the CSM and adding a humidifier to the CSM. A schematic diagram of the tribological test is shown in Figure 1. The humidity sensor in the humidifier ensures that the humidity error is less than 2% RH. The GCr15 balls with a diameter of 6 mm were used as the counterbodies in the friction tests. The tests were performed under a normal load of 5 N at a reciprocating frequency of 2 Hz using an amplitude of 5 mm, which corresponds to an intermediate stress with Hertzian contact pressure of 0.46 GPa to avoid quick fail of the film by friction [25]. All friction tests were repeated at least three times tested under the same conditions to produce consistent results. The average coefficient of friction was calculated for the full sliding process. The wear volume was determined using a non-contact 3D surface profiler (KLA-Tencor, MicroXAM-800), and the wear rate was calculated as $Wr = V/(F \times d)$, where V is the wear volume, F the applied normal force, and d the sliding distance.

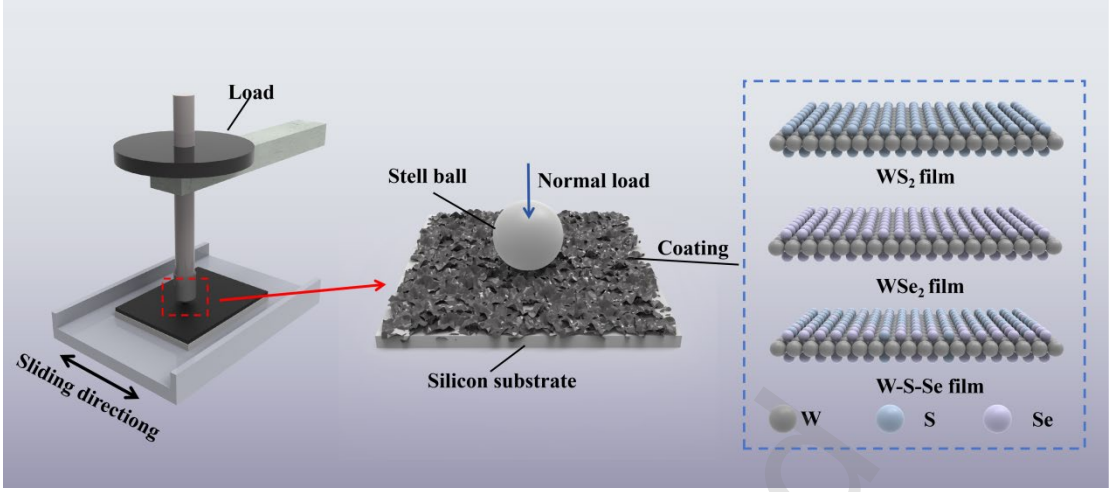

Figure 1. Schematic diagram of tribological testing

2.3 Film characterization

X-ray diffraction (XRD, PANalytical B.V., Empyrean) using Cu K α radiation at an accelerating voltage of 40 kV, and Raman spectroscopy (Jobin Yvon, HR-800) with a 532 nm laser, were employed to characterize the composition and structure of the films. Scanning electron microscopy (SEM, Apreo S) and energy dispersive spectroscopy (EDS) were used to analyze the morphology and composition changes of the films before and after the sliding tests. The microstructures of the films were identified using high-resolution transmission electron microscopy (HR-TEM, FEI Tecnai-G2-F20) operated at 200 kV, with the film sections prepared using the focused ion beam (FIB, Strata 400S) lift-out technique. Before milling, a protective C layer was deposited on the surface of the films to protect the films against beam damage. The film hardness and elastic modulus were estimated by nanoindentation (NHT3, Anton Paar), with a maximum displacement of 60 nm (less than 10% of the film thickness) and a holding time of 5 s.

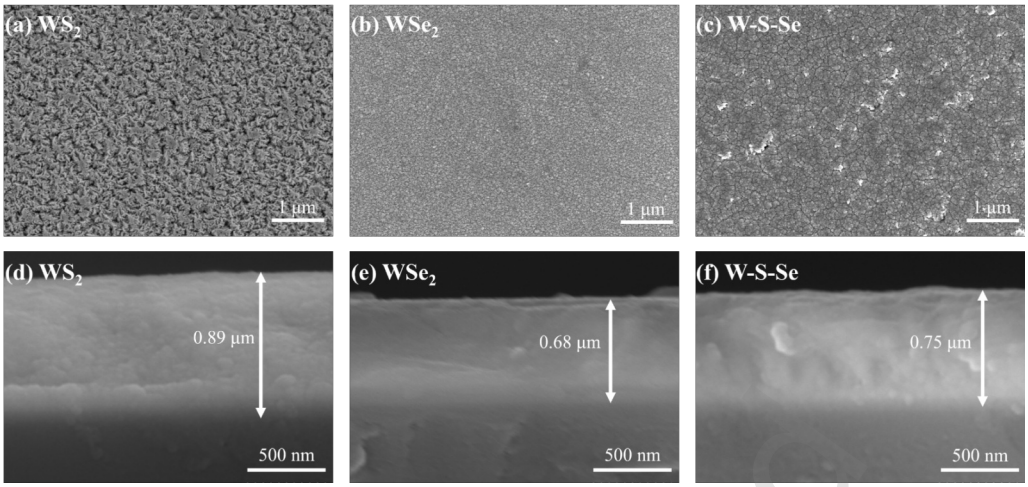

Figure 2. Scanning electron microscope images obtained from the top and cross-sectional areas of the as deposited WS_2 (a, d), WSe_2 (b, e), and W-S-Se (c, f) films.

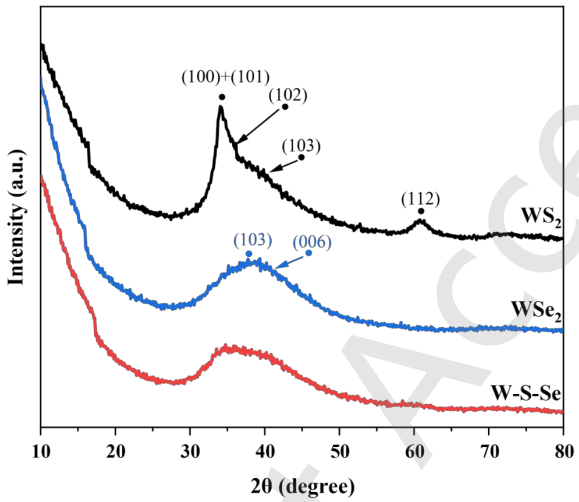

Figure 3. XRD patterns of WS_2, WSe_2, and W–S–Se films. WS_2 exhibits sharp peaks from crystalline planes, while WSe_2 shows a broad amorphous band. Se doping reduces crystallinity, producing a mixed pattern of broad band plus residual WS_2 peak at 36°. This confirms that Se promotes amorphization.

The SEM images taken from the top and cross-sectional areas of the prepared films are shown in Figure 2. The WS_2 surface exhibited a typical dendrite-like structure with a thickness of 0.89 μm, generally related to crystalline structure where WS_2 layers are oriented in a direction normal to the substrate [25, 41]. In comparison, the W-S-Se and WSe_2 films showed transitions from dendrite-like structures to fine structures with film thickness of 0.75 μm for the former and 0.68 μm for the latter. The change in the film structures could also be revealed from the XRD patterns shown in Figure 3. The as

deposited WS_2 film showed well-defined peaks at 2θ of 33° for (100) and (101) planes, and at 2θ of 36°, 40° and 61° for (102), (103) and (112) planes consistent with a crystalline structure. In comparison, the WSe_2 film only showed a broad band centered around 38° primarily contributed by diffraction patterns of (103) and (006) planes, indicating an increased amorphous character. The deposited W-S-Se film shared a similar diffraction band to WSe_2 accompanied with a more significant diffraction peak at 2θ of 36° corresponding to WS_2. Hence, the XRD pattern of W-S-Se revealed Se doping reduced crystallinity of the film, which is similar to the effects of O [15], N [42] and Ag [43] doping in WS_2. It is generally accepted that increased amorphous film with denser structure enhances the hardness of the transition metal dichalcogenides [44]. This trend was observed here with hardness and elastic modulus values of 2.10 GPa and 52.24 GPa for W-S-Se and 3.69 GPa and 68.16 GPa for WSe_2 compared to baseline values of 0.95 GPa and 27.78 GPa for WS_2, as shown in Figure 4.

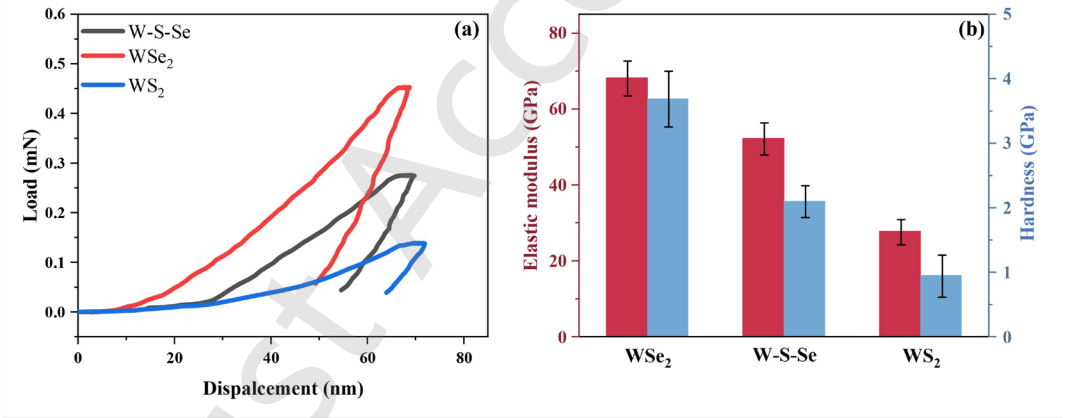

Figure 4. Nanoindentation loading-unloading curves of the prepared films (a), hardness and elastic modulus of the prepared films (b).

2.4 Density functional theory computations

The computations were performed using the Vienna ab initio simulation package (VASP) [45] based on density functional theory (DFT). Projector-augmented wave (PAW) [46] pseudopotentials were used in calculation. The exchange-correlation energy was estimated by the generalized gradient approximation (GGA) using the Perdew-Burke-Ernzerhof (PBE) [47] functional. (4 × 4) cells in dimensions of 13.11 × 13.11 for WS_2 and 13.74 × 13.74 for WSe_2 were used to evaluate the effects of H_2O

adsorption on interlayer adhesion and layer sliding properties. All surface and interfaces of WS_2 and WSe_2 were constructed by adding a 15 Å vacuum layer in direction normal to the basal plane, and the cells were large enough to exclude interactions from periodical images. The vdw-DF2 [48] method was used to describe van der Waals interactions between the layers as presented in Ref.[49, 50]. As in previous simulations, it is foundThe adsorption energy (Ea) of H_2O on WS_2 and WSe_2 was calculated by: $E_a = E_{slab+H_2O} - E_{slab} - E_{H_2O}$, where E_{slab+H_2O} and E_{slab} are the total energies of systems with and without adsorbed H_2O with E_{H_2O} representing the energy of H_2O molecule in the same cell. The interlayer adhesion of WSe_2 was investigated by calculating the interlayer binding energy (E_B) via:$E_B = (E_{layer1} + E_{layer2} - E_{tot})/A$, where E_{layer1} and E_{layer2} represent the energies of isolated layers, and E_{tot} is the total energy of system. For interfaces with H_2O adsorbed, the E_B was calculated by $E_B = (E_{layer1+H2O} + E_{layer2} - E_{tot})/A$, where $E_{layer1+H2O}$ representing layer with H_2O adsorbed was used instead of isolated layer to avoid overestimation of the E_B values due to H_2O interaction with both the upper and lower layers. The plane-wave cut-off energy of 500 eV and a k-point Monkhorst-Pack [51] grid of 5 × 5 × 1 were used to converge the Hellmann-Feynman forces on the atom to less than 0.02 eV/Å and energy to 10^{-5} eV/atom. Spin polarization was considered to address the possible magnetic effect induced by vacancy defects in the cells.

3. Results and discussion

3.1 DFT simulations of Se on inhibiting formation of interfacial hydrogen bonds with H_2O that impeded layer shearing

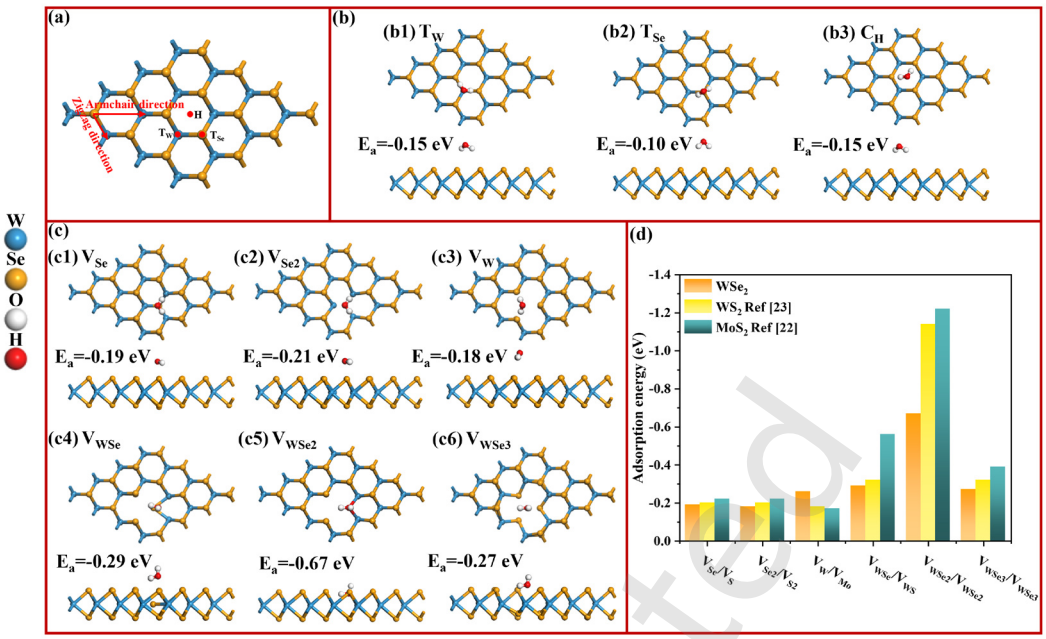

Figure 5. (a) Top view of three high-symmetry adsorption sites for an H_2O molecule on monolayer WSe_2: C_H site (centre of the hexagonal ring), T_W site (on top of W atom), T_{Se} site (on top of Se atom). (b) Top and side views of H_2O molecule adsorbed at high symmetry sites of WSe_2. (c) Top and side views of H_2O molecule adsorbed at different vacancy defects of monolayer WSe_2. (d) Adsorption energy of H_2O molecule on the different vacancy defects of the MoS_2 [24], WS_2 [25] and WSe_2.

To evaluate the adsorption behaviour of H_2O molecules on the surface of WSe_2, various adsorption sites were considered, such as high symmetry sites (See C_H, T_W, T_{Se} sites in Figure 5(a)) and high reactivity vacancy defect sites (V_{Se}, V_{Se2}, V_W, V_{WSe}, V_{WSe2}, V_{WSe3}). For pristine WSe_2, the *Ea* ranges from -0.10 ~ -0.15 eV, where H_2O molecule is more preferably adsorbed at the C_H and T_W sites with the H atoms from H_2O molecule pointing to the Se atoms as displayed in Figure 5(b). The *Ea* values and H_2O orientations are similar to those for H_2O on pristine WS_2 [52]. For H_2O adsorption at vacancy defects of WSe_2, Figure 5(c) showed lower *Ea* values in the range of -0.18 eV ~ -0.67 eV, indicating more stable adsorption states of H_2O on WSe_2 induced by defects. The reactivity of the vacancy defects to H_2O determined from the *Ea* values follows the order of V_{WSe2} (-0.67 eV) > V_{WSe} (-0.29 eV) > V_{WSe3} (-0.27 eV) > V_{Se2} (-0.21 eV) > V_{Se} (-0.19 eV) > V_W (-0.18 eV). H_2O showed almost the same configurations above V_{Se} and V_{Se2} sites with H_2O almost parallel to the basal plane and O atom located above

the Se vacancy, while H_2O molecule at V_W site was shifted from its initial orientation to almost normal to the basal plane with the two O-H bonds pointing towards the two neighboring Se atoms. At V_{WSe} site, the H_2O molecule was normal to the basal plane and 2.02 Å above the Se plane with O on top of Se vacancy site. Notably, under the influence of the interaction between the vacancy and H_2O molecule, the Se atom beneath the vacancy shifted to the W plane. For H_2O adsorbed at V_{WSe2} and V_{WSe3}, the H_2O showed similar orientation as that at V_{WSe}, except the H_2O located closer to the basal plane with a distance of 0.10 Å for the former and 0.94 Å for the latter. It is noted that the H_2O at V_{WSe2} resulted in formation of W-O-W bonds with a bond length of 2.38 Å between the O from H_2O and the neighboring W atoms at defect site while leaving H_2O undissociated, where the increased bonds is responsible for the lowest *Ea* and more stable adsorption. A systematic plots of *Ea* at various vacancy defects in Figure 5(d) showed that the adsorption behavior of H_2O at vacancy defects of WSe_2 resembles those of MoS_2 [24] and WS_2 [25], where the most stable configurations corresponded to formation W-O-W and Mo-O-Mo bonds with bond lengths of 2.36 Å and 2.34 Å at V_{WS2} vacancy of WS_2 and V_{MoS2} vacancy of MoS_2. Overall, under the same type of vacancy computed using the same methodology, the *Ea* values follow the order of $Ea(MoS_2) < Ea(WS_2) < Ea(WSe_2)$, indicating weaker interaction between Se and H_2O molecules. Thus, Figure 5 indicates that while defects enhance H_2O adsorption, the interactions are still weaker on WSe_2 compared to WS_2 and MoS_2, suggesting that Se substitution may help suppress interfacial hydrogen bonding. Our DFT results consistently show that O–H···Se bonds are longer and weaker than O–H···S bonds, leading to reduced charge transfer and lower sliding energy barriers in WSe_2.

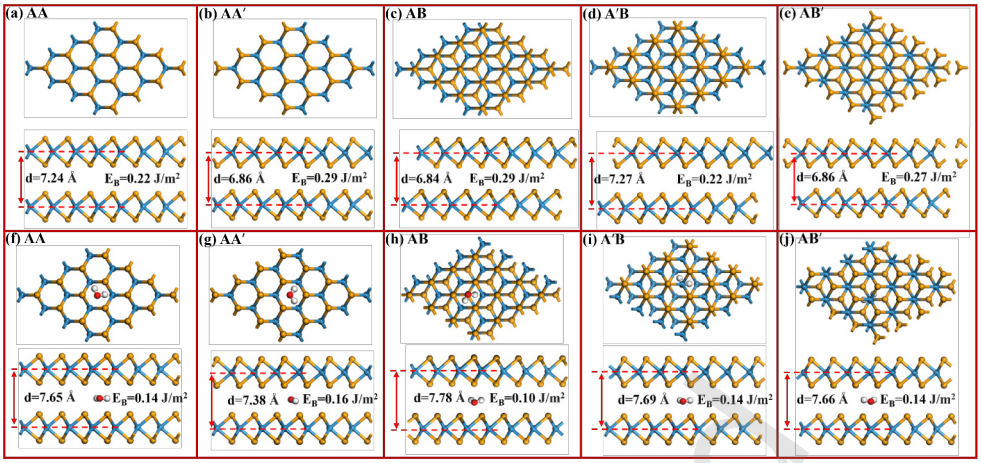

Figure 5. Top and side views of the bilayer WSe_2 without and with intercalated H_2O in stacking sequences of (a, f) AA stack, (b, g) AA′ stack, (c, h) AB stack, (d, i) A′B stack, and (e, j) AB′ stack.

The adhesion properties of the WSe_2 were investigated by calculating E_B values with all five stacking sequences considered, i.e. AA (Mo on Mo), AA′ (Mo on Se), AB (Mo on Se), A′B (Se on Se) and AB′ (Mo on Mo). Both pristine bilayer WSe_2 with and without H_2O intercalated at interfaces were studied to understand how H_2O would affect the interface structures and interlayer adhesion. As shown in Figures 6(a-e), the bilayer WSe_2 in the AA′, AB, and AB′ stacks showed higher E_B values of 0.27 - 0.29 J/m^2 with layer spacings of 6.84 - 6.86 Å than those of 0.22 J/m^2 for both the AA and A'B stacks with increased layer spacings of 7.24 Å and 7.27 Å. These results are in agreement with the calculations by He et al [53]. Figure 5 illustrates that intercalation of H_2O expands the interlayer distance by ~0.5 Å and reduces E_B by nearly half (to 0.10–0.16 J/m²), demonstrating that water incorporation strongly perturbs interface stability. Table 2 further confirms that this reduction in adhesion is more severe for WS_2 than for WSe_2, suggesting that Se substitution stabilizes the layered structure against humidity. Intercalating H_2O at the pristine bilayer WSe_2 reduced the E_B from 0.22 J/m^2 ~ 0.29 J/m^2 to 0.10 J/m^2 ~ 0.16 J/m^2, which was accompanied by layer expansions from 6.84 Å ~ 7.24 Å to 7.38 Å ~ 7.65 Å (See Figures 6(f-j)). This layer expansion and reduced E_B seem to be beneficial for friction, but this process is unlikely to occur as the H_2O intercalation process would require extra energy of 0.58 eV ~ 1.18 eV to overcome van der Waals interaction during layer expansion. Although this

phenomenon is unlikely to occur, it can be used to analyze the effect of water molecules on the WS_2 and WSe_2 interfaces. It can be found the E_B values are of the same levels for pristine bilayer WS_2 and WSe_2 with and without intercalated H_2O in Table 2. However, the WS_2 interface is more affected by water molecules, and the extent of interlayer spacing expansion is larger than that of WSe_2.

Table 2. Interlayer binding energy (E_B) and interlayer spacing (d) of bilayer WX_2(X=S, Se) with and without intercalated H_2O.

System		WSe_2 bilayer interfaces		WS_2 bilayer interfaces	
		d (Å)	E_B (J/m^2)	d (Å)	E_B (J/m^2)
AA	Pristine/ Pristine	7.24	0.22	6.90	0.22
	Pristine-H_2O/Pristine	7.65	0.14	7.35	0.13
A′B	Pristine/ Pristine	7.27	0.22	6.89	0.23
	Pristine-H_2O/Pristine	7.69	0.14	7.36	0.13
AA′	Pristine/ Pristine	6.86	0.29	6.46	0.31
	Pristine-H_2O/Pristine	7.38	0.16	7.12	0.14
	V_{WX2}/ V_{WX2}	6.81	0.28	6.40	0.30
	V_{WX2}-H_2O/Pristine	6.83	0.29	6.47	0.32
	V_{WX2}-H_2O/H_2O-V_{WX2}	6.81	0.31	6.41	0.32
AB′	Pristine/ Pristine	6.86	0.27	6.49	0.29
	Pristine-H_2O/Pristine	7.66	0.14	7.48	0.12
	V_{WX2}/ V_{WX2}	6.80	0.27	6.38	0.29
	V_{WX2}-H_2O/Pristine	6.86	0.28	6.45	0.30
	V_{WX2}-H_2O/H_2O-V_{WX2}	6.81	0.29	6.42	0.32
AB	Pristine/ Pristine	6.84	0.29	6.46	0.30
	Pristine-H_2O/Pristine	7.78	0.10	7.33	0.13
	V_{WX2}/ V_{WX2}	6.82	0.28	6.36	0.30
	V_{WX2}-H_2O/Pristine	6.84	0.29	6.42	0.31
	V_{WX2}-H_2O/H_2O-V_{WX2}	6.82	0.29	6.42	0.30

As defects could promote molecule adsorption and stabilize the molecule at interface, the most reactive defect of V_{WSe2} was considered for constructing WSe_2 interfaces with and without adsorbed H_2O in AA′, AB, and AB′ stackings due to their highest E_B values. As shown in Table 2, V_{WSe2} vacancy defect slightly reduced the E_B by 0.01 J/m^2 compared to the pristine WSe_2, while the interlayer spacing varied only marginally between 0.02 and 0.06 Å. The E_B values increased to 0.29 J/m^2 for interfaces with one intercalated H_2O at the interfaces and further to 0.29 - 0.31 J/m^2 with two intercalated H_2O molecules, consistent with the trend observed for H_2O intercalated between WS_2 layers (Table 2). It should be noted that the E_B values for WSe_2 layers with H_2O adsorbed at V_{WSe2} defect sites were 0.01 - 0.03 J/m^2 lower than their counterparts of WS_2 interfaces in the same stackings. However, WSe_2 exhibits better

tribological properties than WS_2 in humid environments likely due to weaker O–H···Se interactions compared to O-H···S.

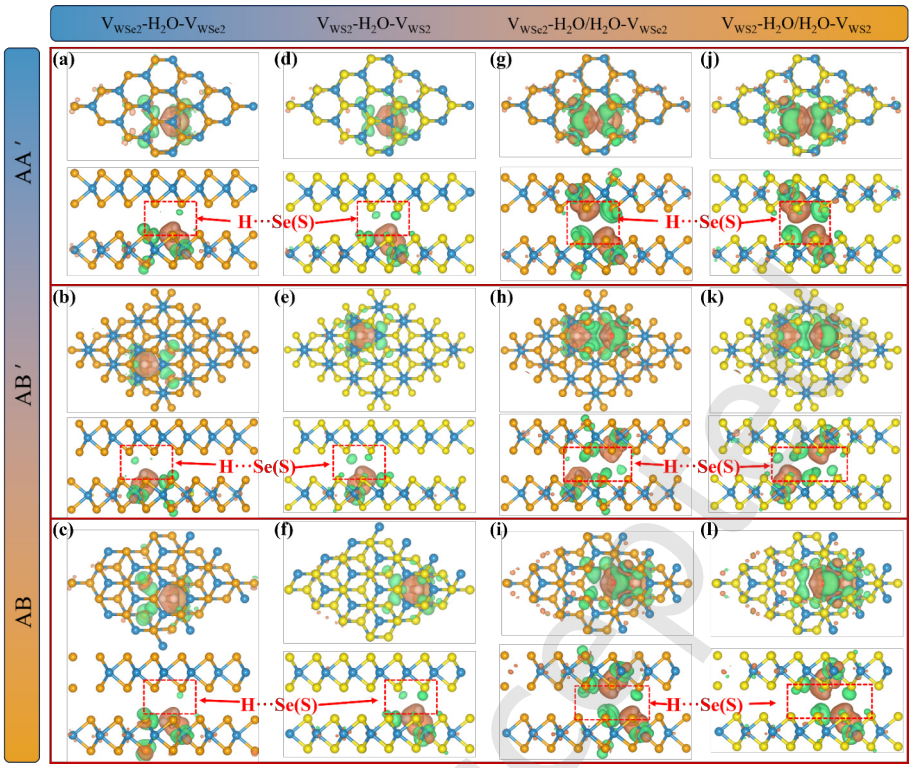

Figure 6. Top and side views of charge density difference (CDD) plots for bilayer configurations of (a-c) WSe_2-H_2O/WSe_2, (d-f) WS_2-H_2O/WS_2, (g-i) WSe_2-H_2O/H_2O-WSe_2, and (j-l) WS_2-H_2O/H_2O-WS_2 in AA′, AB′, and AB stacks. The isosurface value was 0.0015 e/Bhor^3, and the orange and green zones represent charge accumulation and depletion, respectively.

To further clarify the effect of water molecule adsorption on WS_2 and WSe_2 interfaces, charge density difference (CDD) analysis was performed to reveal the associated changes in electron transfer behaviour. As can be seen from the CDD contour plots of WSe_2-H_2O/WSe_2, WS_2-H_2O/WS_2, WSe_2-H_2O/H_2O-WSe_2, and WS_2-H_2O/H_2O-WS_2 in AA′, AB′, and AB stacks, the charge depletion zones (green zones) near S and Se atoms could be identified from both the upper and lower layers of WSe_2 and WS_2 bilayer interfaces. Meanwhile, the charge accumulations zones are shown near the H atom from H_2O at vacancy defects. It should be noted that the charge depletion zones near S atoms were substantially larger than those near Se atoms, which would consequently lead to stronger interaction between the H_2O and S atoms than that with

S atoms. To reach deeper insights into the reduced E_B values between WSe_2 layers, the net charge transfer between H_2O and WS_2 and WSe_2. As shown in Table 3, there are more charge transfer between H_2O and WS_2 than that with WSe_2. Moreover, the bond lengths of O-H···Se bonds (3.02 Å~ 3.25 Å) were larger than those of O-H···S (2.80 Å~ 2.98 Å). According to the bond length and bond angles summarized in Table 3, it can be inferred that the O-H···Se is a weaker hydrogen bonds as the bond length and strength were substantially lower than O-H···S, although the H_2O configurations at the WSe_2 interface are highly similar to that at WS_2 interfaces. In addition, it could be noted from Figure 7 that an increase in the number of H_2O molecules at interfaces would induce more the charge accumulation and stronger interfacial interactions. These interactions would lower the system energy and raise the E_B values by 0.01 J/m^2 and 0.01 J/m^2 ~ 0.02 J/m^2 for WSe_2 interfaces with one and two intercalated H_2O molecules, compared to 0.01 J/m^2 ~ 0.02 J/m^2 and 0 J/m^2 ~ 0.02 J/m^2 for WS_2 interfaces with one and two intercalated H_2O molecules. The charge state of hydrogen atoms in water molecules was analyzed using Bader charge analysis. As shown in Table 3, the number of H atom charge transfers in the WSe_2 interface is generally larger than that in WSe_2. This pronounced difference may be originated from the higher electronegativity of S than that for Se, as well as the difference in their atomic radius. In summary, the CDD analysis and bond length statistics (Figure 7, Table 3) confirm that O–H···Se bonds are weaker than O–H···S bonds, leading to reduced charge transfer and weaker water–film interactions in WSe_2 compared to WS_2. To understand how these differences in interfacial bonding translate into sliding behavior and friction, layer sliding simulations were carried out, as shown in Figure 8.

Table 3. Bond lengths and bond angles and average charge transfer per H atom in interfacial H_2O molecules for WS_2 and WSe_2 bilayers in different stackings.

System		Bond length O-H···Se(S) (Å)	Bond angle O-H···Se(S) (°)	$\overline{\Delta Q}_H$ (e)
AA′	V_{WSe2}-H_2O/Pristine	3.22	148.00	-0.600
	V_{WSe2}-H_2O/H_2O-V_{WSe2}(down)	3.02	148.28	-0.602
	V_{WSe2}-H_2O/H_2O-V_{WSe2}(up)	3.02	148.27	-0.612
	V_{WS2}-H_2O/Pristine	2.94	147.77	-0.613
	V_{WS2}-H_2O/H_2O-V_{WS2}(down)	2.88	144.70	-0.618
	V_{WS2}-H_2O/H_2O-V_{WS2}(up)	2.88	144.60	-0.614

AB′	V_{WSe2}-H_2O/Pristine	3.15	162.02	-0.602
	V_{WSe2}-H_2O/H_2O-V_{WSe2}(down)	3.12	162.74	-0.610
	V_{WSe2}-H_2O/H_2O-V_{WSe2}(up)	3.12	162.60	-0.607
	V_{WS2}-H_2O/Pristine	2.83	163.87	-0.609
	V_{WS2}-H_2O/H_2O-V_{WS2}(down)	2.80	163.90	-0.628
	V_{WS2}-H_2O/H_2O-V_{WS2}(up)	2.80	163.95	-0.629
AB	V_{WSe2}-H_2O/Pristine	3.25	148.17	-0.596
	V_{WSe2}-H_2O/H_2O-V_{WSe2}(down)	3.09	148.78	-0.589
	V_{WSe2}-H_2O/H_2O-V_{WSe2}(up)	3.12	139.18	-0.590
	V_{WS2}-H_2O/Pristine	2.92	146.69	-0.612
	V_{WS2}-H_2O/H_2O-V_{WS2}(down)	2.86	145.96	-0.620
	V_{WS2}-H_2O/H_2O-V_{WS2}(up)	2.98	137.61	-0.611

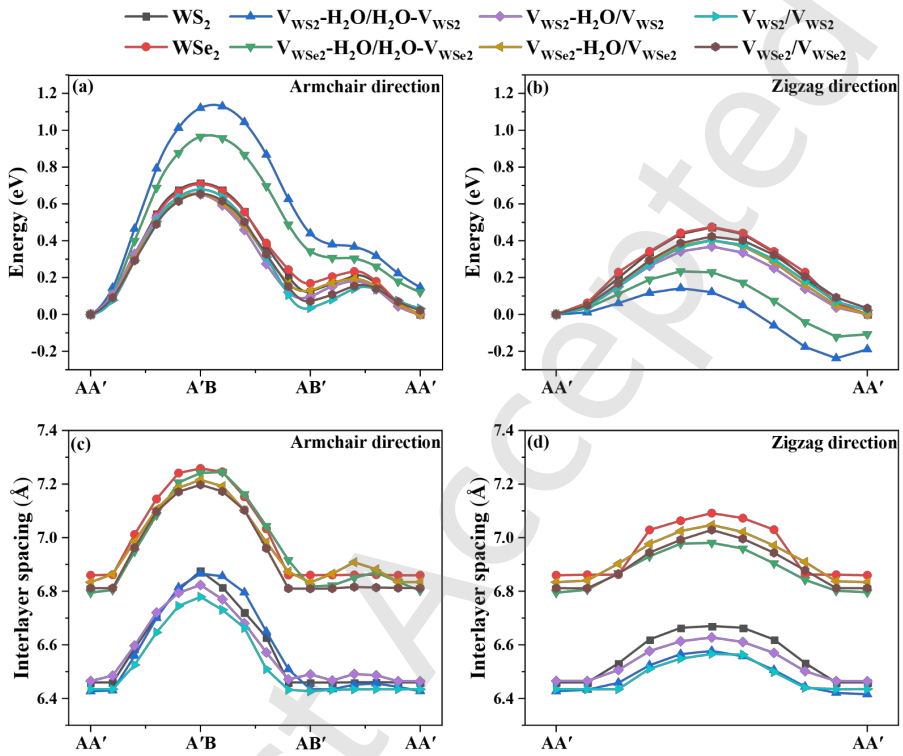

Figure 8. (a, b) Sliding energy barriers of bilayer WS_2 and WSe_2 with and without interfacial H_2O in the armchair and zigzag directions. (c) Interlayer spacing variations corresponding to the sliding configurations.

In order to understand how the changes in E_B values translate into layer sliding and friction performance, the layer sliding properties was simulated by sliding both pristine and vacancy defected WS_2 and WSe_2 layers without and with one or two adsorbed H_2O molecules at the interfaces along the sliding direction shown in Figure 5(a). The relative energy changes along the sliding direction shown Figure 8(a, b) revealed almost the sliding energy barrier for pristine WS_2 (0.71 eV in armchair and 0.47 eV in Zigzag) and WSe_2 (0.70 eV in armchair and 0.48 eV in zigzag). The presence

of V_{WX2}(X=S, Se) vacancies reduces the sliding energy barriers of WS_2 and WSe_2 in the armchair direction to 0.68 eV and 0.65 eV, respectively, and in the zigzag direction to 0.40 eV and 0.42 eV, respectively. Furthermore, the adsorption of a water molecule in the V_{WX2}(X=S, Se) vacancy has no significant effect on the sliding energy barrier in zigzag direction.

However, when water molecules are adsorbed on the upper and lower interfaces of WX_2, the sliding energy barrier is significantly affected. In the zigzag direction, the sliding energy barriers for WS_2-H_2O/H_2O-WS_2 and WSe_2-H_2O/H_2O-WSe_2 are 0.14 eV and 0.23 eV, respectively. The decrease in the energy barrier values is due to the fact that the sliding paths in the zigzag direction deviate from the high symmetry stacks and the atomic stacks formed are mostly relatively misaligned structures. That prevents the water molecules from stabilizing the formation of a hydrogen bonding network, at which time the water molecules are present at the interface as spacers, reducing the direct contact at the WX_2(X=S, Se) interface and thus the sliding energy barrier. In the Armchair direction, the sliding energy barriers were increased by 0.42 eV to 1.13 eV for WS_2-H_2O/H_2O-WS_2 and by 0.26 eV to 0.96 eV for WSe_2-H_2O/H_2O-WSe_2. The energy barriers were all met during sliding process that reached the A′B stack, which correspond to the stack of X on X for WX_2(X=S, Se). The layer spacing changes displayed in Figure 8(c) showed the largest layer expansions for the interfaces in A′B stack owing to the repulsion between the S(Se) planes. The layer spacings between bilayer WS_2 and bilayer WSe_2 at the energy barrier configurations were 6.88 Å and 7.26 Å, which were almost the same as those of 6.86 Å and 7.24 Å for WS_2-H_2O/H_2O-WS_2 and WSe_2-H_2O/H_2O-WSe_2. Hence, it can be inferred that the sliding process in the simulated system with H_2O adsorbed at vacancy defect sites was affected by the interaction between H_2O and Se for WSe_2 and S for WS_2, as the changes in the layer spacing indicate almost no difference between the computed interfaces with and without adsorbed H_2O corresponding to van der Waals interactions. Thus, the layer sliding simulations showed H_2O was less effective on impeding the layer shearing for WSe_2 than WS_2, which is consistent with the E_B values and CDD analyses. Figure 8 therefore demonstrates that water molecules affect sliding anisotropically—reducing

barriers in the zigzag direction but increasing them in the armchair direction—yet the overall penalty of H_2O is less severe in WSe_2 than in WS_2, consistent with weaker O–H···Se interactions.

In summary, the differences in electronegativity and atomic radius between S and Se result in variations in the strength of the interface hydrogen bonds formed between WS_2, WSe_2, and water molecules. Therefore, in the experiment, Se was introduced into WS_2 to alter its interface electronic structure, and the W–S–Se interface hydrogen bonding network was adjusted through the differences between S and Se. Thereby reducing the interaction between the W–S–Se film and water molecules. In the following subsection, the effect of Se doping on mitigating the friction sensitivity to humid air was explored by performing sliding friction experiments in humid environments.

3.2 Tribological behaviour of WS_2, WSe_2, W-S-Se films in dry and humid air

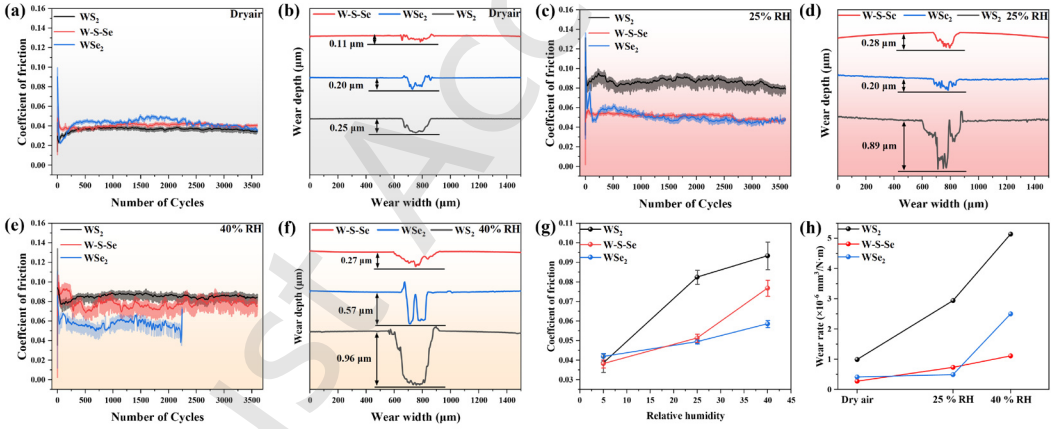

Figure 9. Curve of coefficient of friction with number of cycles and cross-sectional wear depth plots of WS_2, WSe_2 and W-S-Se films under different humidity conditions: (a-b) dry air, (c-d) 25% RH, (e-f) 40% RH. Variation curves of (g) coefficient of friction and (h) wear rates with relative humidity for WS_2, WSe_2 and W-S-Se films.

To verify the effect of Se on inhibiting friction increase in humid environments by forming hydrogen bonds that increase the layer adhesion and impeded layer shearing, sliding tests of WS_2, WSe_2, W-S-Se in air with different humidity levels were performed, i.e. dry air, 25% RH, and 40% RH. Firstly, the friction curves in Figure 9(a) showed a common low COF of ~0.04 for all the three films. This result is consistent

with the sliding simulations where both WS_2 and WSe_2 showed an identical sliding energy barrier of ~0.70 eV. Meanwhile, the profiles of the wear tracks of the films after tests in Figure 9(b) showed a decrease in the wear depth from 0.25 μm for WS_2 to 0.20 μm for WSe_2, and further to 0.11 μm for W-S-Se. Due to the low hardness of 0.95 GPa, the wear rate of WS_2 is the highest among the three films, with the maximum wear depth and highest specific wear rate of 0.99×10^{-6} $mm^3/N\cdot m$. It is interesting to note the W-S-Se film, with hardness of 2.10 GPa showed lower wear than WSe_2 which had the highest hardness of 3.69 GPa. This indicates that increasing the hardness beyond a certain level may not necessarily reduce wear in dry environments. Overall, W-S-Se film showed the best tribological performance in the dry environment, possibly due to its improved hardness without sacrificing the lubricity of the layered structure. Thus, simply increasing hardness (as in WSe_2) does not ensure lowest wear; rather, Se-doped WS_2 (W–S–Se) optimizes both hardness and layered lubricity, achieving the best performance in dry sliding.

With the humidity level raised to 25% RH, the COFs of WS_2, WSe_2, and W-S-Se were subjected to different increases due to different levels of moisture sensitivity of the films. As can be seen in Figure 9(c), WS_2 experienced the most significant increase in COF from 0.04 in dry air to 0.08. Meanwhile, the COFs of WSe_2 and W-S-Se only increased slightly to a common low value of 0.05 compared to the low value of 0.04 in dry air, confirming the effect of Se on inhibiting the film sensitivity to moisture. The 2D wear profiles of the three films corresponding to the friction curves in Figure 9(d) showed substantially smaller wear depths for WSe_2 (0.20 μm) and W-S-Se (0.28 μm) than the 0.89 μm depth observed for WS_2, corresponding to specific wear rates reductions from 2.94×10^{-6} $mm^3/N\cdot m$ for WS_2 to 0.49×10^{-6} $mm^3/N\cdot m$ for WSe_2 and 0.73×10^{-6} $mm^3/N\cdot m$ for W-S-Se.

The effectiveness of Se doping on enhancing the film resistance to tribological performance degradation induced by H_2O molecules could be better manifested from sliding tests performed in air with 40% RH. As shown in Figure 9(e, f), both the COF and wear depth of WS_2 (0.96 μm） are the highest compared to those of WSe_2 and W-S-Se. It is noted that the COF of WSe_2 increased slightly further to 0.06 but suffered

from film failure after ~2200 cycles due to its lowest film thickness. The COF of the W-S-Se film increased to ~0.08, which is slightly lower than WSe_2. However, the wear depth of the former (0.27 μm) is less than half of WSe_2 (0.57 μm).

The above friction and wear results are summarized in Figure 9(g, h), where WSe_2 showed the lowest moisture induced friction increase and WS_2 the highest friction increase with humidity. While the W-S-Se film showed intermediate friction increase with humidity, it exhibited the lowest specific wear rate of 1.11×10^{-6} $mm^3/N\cdot m$ representing a reduction of 56% and 78% compared to 2.50×10^{-6} $mm^3/N\cdot m$ for WSe_2 and 5.14×10^{-6} $mm^3/N\cdot m$ for WS_2. These results clearly demonstrate that Se doping enhanced the resistance of the WS_2 films to humidity-induced degradation in both dry and humid air. The worn surfaces were analyzed in the following sub-section to illustrate the underlying mechanism.

3.3 Worn surface analyses

The transfer layers formed on the worn scars of the steel balls (counterfaces) were analyzed using SEM coupled with EDS mapping, as the TMD transfer layer are an essential factor controlling the friction process by creating an interface that prevents direct contact between the metal surfaces. As can be seen in Figure 10, the diameter of the wear scars of WS_2 increased from 157 μm in dry air to 226 μm and 264 μm at 25% RH and 40% RH respectively, whereas those of WSe_2 remained mainly unchanged at ~165 μm in dry air and 25% RH under the same testing conditions. The larger wear scar diameter of 238 μm of WSe_2 tested at 40% RH could be to increased friction after partial film failure. In addition, the formation of WS_2 and WSe_2 transfer layers can be identified from the W, S, and Se elemental maps. It could also be noted that the O overlapping with those of W and S from WS_2 film becomes more obvious with increasing humidity level, while in WSe_2 films such overlap with O is insignificant. The low W and Se coverage with high O signal in Figure 10(d) for WSe_2 tested at 40% RH likely arises from severe wear and film failure leading to iron oxide formation from the exposed substrate. These observations agree with the computational results predicting that H_2O adsorption is stronger on WS_2 than WSe_2 (either dissociated or

undissociated) which consequently forms weaker interfacial bonds and makes friction of WSe_2 less sensitive to humid environment.

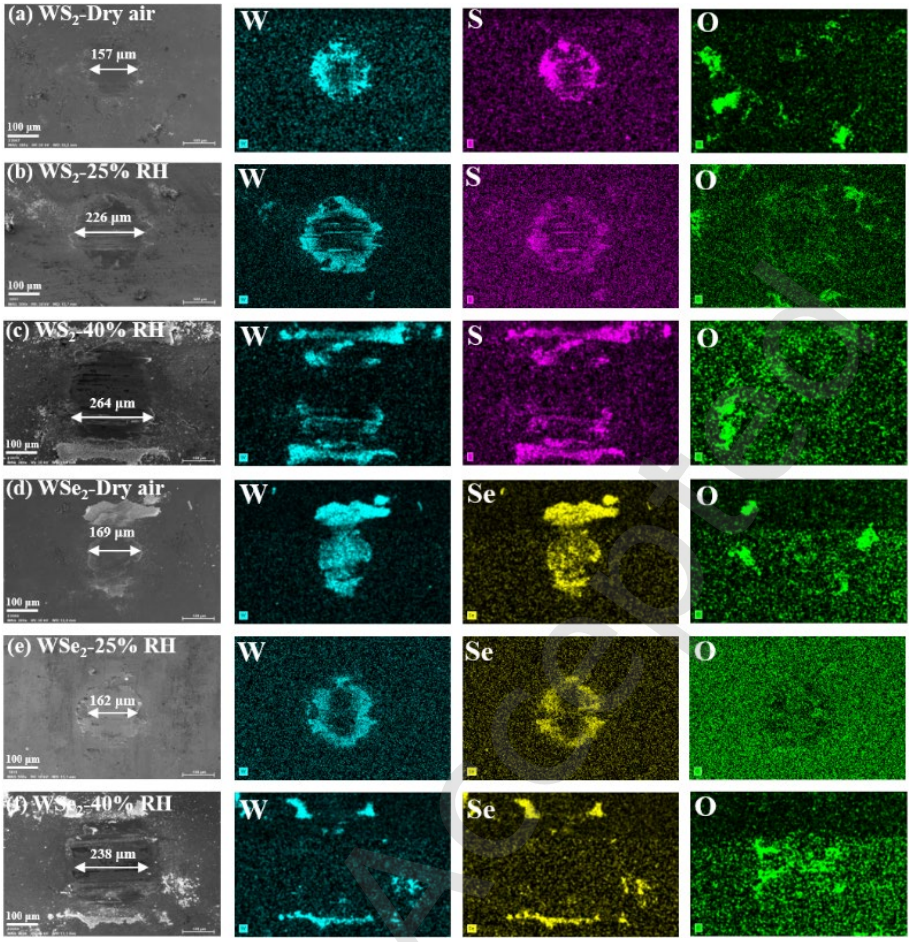

Figure 10. SEM images and EDS maps of the wear scars on steel ball surfaces during sliding against WS_2 at (a) dry air, (b) 25% RH, (c) 40% RH; and against WSe_2 at (d) dry air, (e) 25% RH, (f) 40% RH.

In alignment with the friction results, the wear scars on steel balls tested against the W–S–Se film showed the smallest diameters under both dry and humid conditions, indicating reduced sensitivity to moisture-induced degradation. As shown in Figure 11, the diameter of the wear scars in all the testing conditions were the smaller compared to those for both WS_2 and WSe_2, increased modestly from 141 µm in dry air to 152 µm and 211 µm in at 25% RH and 40% RH respectively. Similar to WSe_2, the W-S-Se transfer layer could be clearly identified from the W, S, Se elemental maps, while O enrichment was minimal. However, unlike WSe_2 tested at 40% RH where no transfer layer remained on the wear scar, the central region of the wear scars on steel sliding

against W-S-Se film retained a relatively more uniform transfer layer. These SEM/EDS analyses therefore indicate that the W–S–Se film is less sensitive to moisture adsorption than WS_2 and exhibits better tribological stability in humid environments than WSe_2, consistent with the friction and wear data in Figure 9.

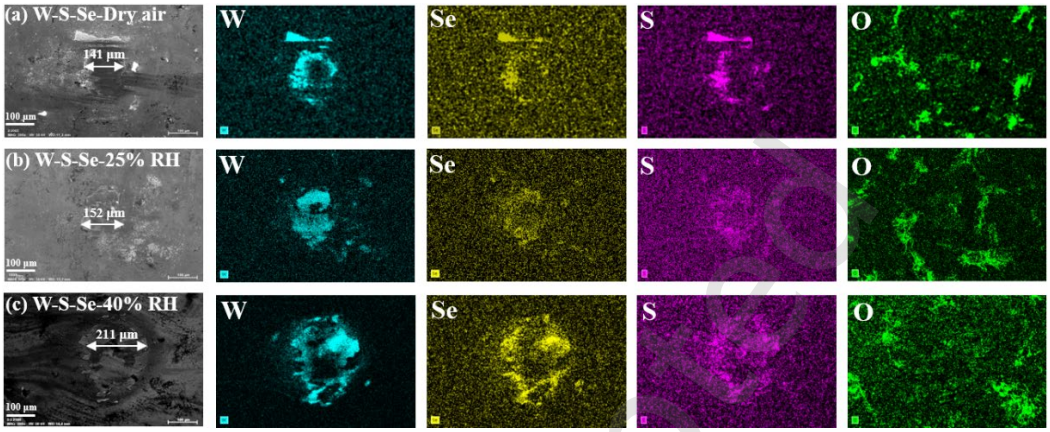

Figure 11. SEM images and EDS maps of the wear scars on steel ball surfaces sliding against W-S-Se at (a) dry air, (b) 25% RH, (c) 40% RH.

In order to understand the effect of water molecules on the compositional changes in WS_2, WSe_2 and W-S-Se films, i.e. potential oxidation of the film during the sliding tests, the films before and after sliding were analyzed by Raman spectroscopy. As shown in Figures 12(a, b), both the WS_2 and WSe_2 on wear tracks and on wear scars (transfer layers) exhibited the Raman peaks around 350 cm^{-1} and 420 cm^{-1} corresponding to the $E_{2g}{}^1$ and A_{1g} modes of WS_2 [54] and the peaks at 249 cm^{-1} and 259 cm^{-1} for the $E_{2g}{}^1$ and A_{1g} modes of WSe_2 [55], similar to those of the as deposited films. In comparison, Raman peaks for WS_2 and WSe_2 in W-S-Se film displayed in Figure 12 (c) were relatively weak in the as deposited state, but became more pronounced in the transfer layers on the wear tracks after sliding in both dry and humid environments. These changes in the Raman peaks of W-S-Se film could be attributed to more layered structures in the transfer layer. It is also noted that no significant Raman peaks of WO_3 or SeO_2 were observed on the wear scars or wear tracks of the WS_2, WSe_2, and W–S–Se films, indicating that while some oxidation cannot be excluded, it does not play a dominant role in the tribological response under humid conditions, consistent with DFT results showing that interfacial water adsorption governs the humidity effect. Taken

together, these Raman observations, along with the friction, wear, and transfer layer analyses, are consistent with the DFT results showing that Se substitution weakens water–film interactions, thereby reducing the humidity sensitivity of WS_2.

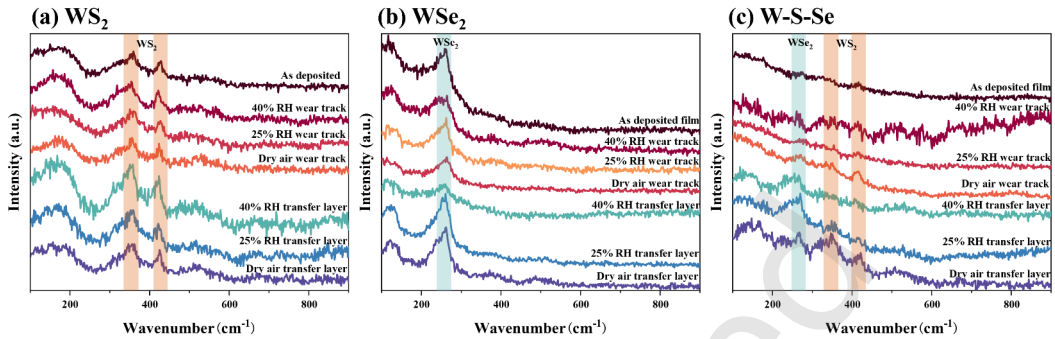

Figure 12. Raman spectra of wear scars and wear tracks in (a) WS_2, (b) WSe_2 and (c) W-S-Se, in comparison with the as deposited films.

The cross-sectional microstructure of the W-S-Se film before and after sliding tests was characterized by TEM using FIB lift out technique. As shown in Figures 13 (a, b), the W-S-Se film exhibited a typical columnar morphology with layers containing amorphous zones, similar to WS_2 and MoS_2 films deposited by magnetron sputtering [21, 24, 25]. This indicates that Se doping does not alter the fundamental growth mode of the film. Compared to the as deposited W-S-Se film where the layers were misoriented, the W-S-Se transfer layer displayed in Figure 13 (c) showed parallel re-oriented layers along the sliding direction. It is also noted that the amorphous zones presented in the as deposited film are barely observable in the transfer layer, which may be related to friction induced the crystallization of the amorphous TMD layers. This friction-induced structural reorganization dominates the interfacial characteristics where shear actually occurs, thereby significantly weakening the secondary influence of the initial crystallinity variations and associated defect differences on the friction behavior. The increased number of rings in the selected area electron diffraction image insert of Figure 13 (d) compared to Figure 13 (b) indicating that the transfer layer is more crystalline than the as-deposited film. Although it is challenging to directly distinguish WSe_2 layers from WS_2 in the transfer layer, the distinct difference of the layer spacings provide an approach. As shown in Figure 13 (d) that the transfer layers mainly consist of spacings of ~0.66 nm for WS_2 and ~0.75 nm for WSe_2. It should be

noted S substitution by Se may be widely present within the WS_2 layers, and vice versa. The shearing of these layers could be responsible for the improved performance of W-S-Se film. Furthermore, sliding induces local reorientation of the layered structure in the transfer layer, resulting in parallel-aligned lamellae along the sliding direction [24, 56]. This friction-induced lattice rearrangement effectively reproduces the atomic-scale anisotropic sliding behavior predicted by our DFT calculations, linking the observed microscopic structural evolution to the macroscopic tribological performance of the W–S–Se film.

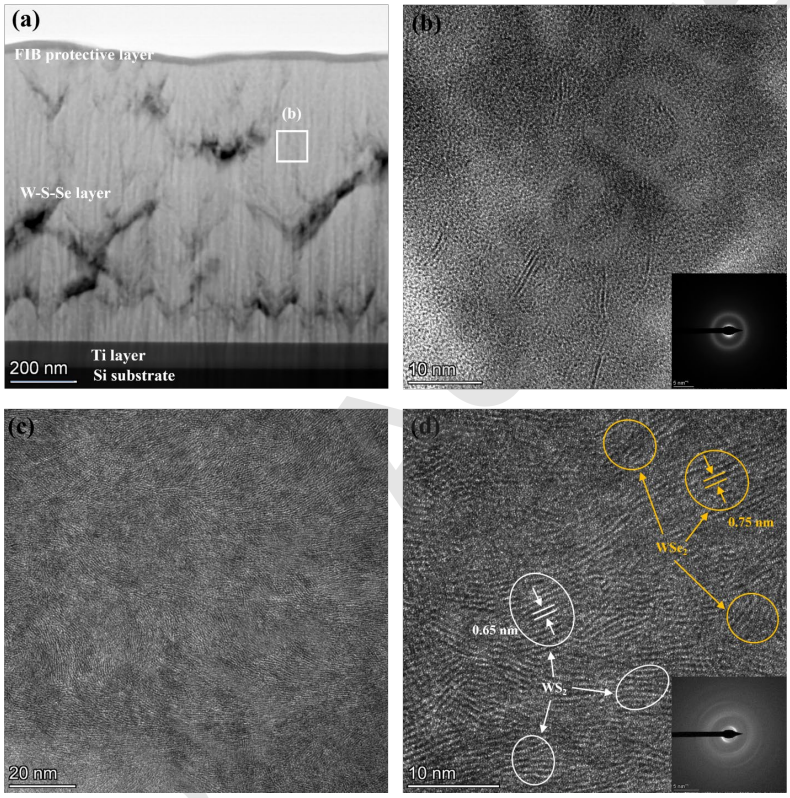

Figure 13. Cross-sectional TEM (a) and HR-TEM (b) of the as-deposited W–S–Se film, showing columnar growth with amorphous zones. (c, d) Cross-sectional HR-TEM of the transfer layer formed on the steel surface after sliding at 25% RH, revealing re-oriented parallel layers with reduced amorphous regions. Distinct lattice spacings of ~0.66 nm (WS_2) and ~0.75 nm (WSe_2) confirm Se incorporation, while sharper SAED rings indicate enhanced crystallinity of the transfer layer.

In summary, the worn surface analyses showed that oxidation of the three films is insignificant with no observable WO_3 detected by Raman and TEM. While the COF of WS_2 is known to depend strongly on humidity with WSe_2 being less sensitive to moisture and exhibiting lower friction the WSe_2 film nevertheless experienced more severe wear under higher humidity (40% RH), whereas Se-doped WS_2 balances both properties. The mechanism of friction increase by moisture for MoS_2 and WS_2 has been revealed by the authors' previous work, where adsorption of H_2O molecules at the interfaces would form O-H···S type of interfacial bonds that increased the E_B and impeded layer shearing [21, 24, 25]. In this work, DFT computations showed that although WSe_2 exhibits E_B values comparable to WS_2 its larger layer spacing and lower E_B upon H_2O adsorption correspond to weaker O–H···Se bonds and a lower sliding energy barrier. The W–S–Se films verified the effectiveness of Se doping, showing inhibited degradation of tribological performance under both low and high humidity levels. Sliding experiments confirmed that the W–S–Se film exhibited the lowest friction and wear across both dry and humid environments. The formation of parallel layers at the interface was similar to that observed in MoS_2 and WS_2. Therefore, this study revealed the effectiveness of Se doping in inhibiting the formation of interfacial hydrogen bonds and improving the tribological performance.

4. Summary and Conclusions

Friction of transition metal dichalcogenides is known to increase with exposure to humidity due to adsorption of H_2O molecules at interfaces that form interfacial hydrogen bonding. Using DFT computation coupled with sliding experiments, this paper investigates the mechanism differentiating the tribological properties of WS_2 and WSe_2 under humid conditions and explores how Se doping into WS_2 can inhibit the formation of interfacial bonding for improved tribological performance in humid environments. The main conclusion drawn from this study are as follows:

1. DFT studies showed that WSe_2 has an E_B value comparable to WS_2, but it increases slightly once with H_2O adsorbed at the interface, whereas that of WS_2 increases more significantly due to formation of O-H···S hydrogen bonds. The

interfacial sliding simulation showed that the sliding energy barrier of bilayer WSe_2 increases less than that of WS_2

2. The Se-doped W–S–Se film was prepared by magnetron sputtering using a WS_2/WSe_2 composite target, exhibited a higher hardness of 2.10 GPa than that of 0.95 GPa for WS_2, but lower than that of 3.69 GPa for WSe_2. Sliding friction revealed that the W-S-Se film showed the lowest friction and wear rates across both dry and humid environments, with 40% RH compared to pure WS_2 and WSe_2.

3. The W-S-Se transfer film exhibited layer parallel re-oriented lamellae with a layer spacing larger than that of pure WS_2. This coupled with the weaker interfacial O-H···Se hydrogen bonds compared to O-H···S, contributed to the enhanced tribological performance of the W-S-Se film in both dry and humid environments.

This study demonstrates that the friction and wear of TMDs in the presence of water are not fixed material properties but can be rationally designed by controlling hydrogen bond strength at the atomic level. The concept of doping to modulate interfacial water interactions opens a generic and powerful avenue for developing next-generation lubricants capable of operating reliably across a wide spectrum of environmental conditions.

Credit authorship contribution statement

Yuqian Huang: Investigation, Data curation, Writing original draft. Bin Zhang: Investigation, Writing original draft. Zhiwei wang: Investigation, Zaixiu Yang: Conceptualization, Methodology, Writing-review & editing. Zhenwei Niu: Formal analysis. Kaixiong Gao: Funding acquisition. Junyan Zhang: Supervision. Goksel Hizli: Formal analysis, Writing – review & editing. Kürşat Kazmanlı: Formal analysis, Writing – review & editing. Ahmet Alpas: Conceptualization, Writing – review & editing, Software.

Declaration of Competing Interest

The authors declare that they have no known competing financial interests or personal relationships that could have appeared to influence the work reported in this paper.

Data Availability

Data will be made available on request.

Acknowledgments

This work was supported by the National Key Research and Development Program of China (No. 2023YFB3712300), the National Natural Science Foundation of China (52105227), Youth Fund of Key Laboratory of Science and Technology on Wear and Protection of Materials from Chinese Academy of Science (SYSQJ-2022-1), the CAS "Light of West China" Program. Financial support received from the Natural Sciences and Engineering Research Council of Canada (NSERC) is also gratefully acknowledged (06340-2018).

References

[1] Huang X, Zeng Z Y, Zhang H. Metal dichalcogenide nanosheets: preparation, properties and applications. Chem Soc Rev 2013;42:1934-1946.

[2] Jamison W E, Cosgrove S L. Friction Characteristics of Transition-Metal Disulfides and Diselenides. Asle Trans 1971;14:62-72.

[3] Kim B Y, Ahn H J, Bak J S, Choi C H, Ioki K, Zauner C. Lubricant coating of dowel for the ITER vacuum vessel gravity support. Fusion Eng Des 2012;87:1079-1084.

[4] Shi S S, Song Y T, Cheng Y, Villedieu E, Bruno V, Feng H S, Wu H P, Wang P, Hao Z W, Li Y, Wang K, Pan H T. Conceptual design main progress of EAST Articulated Maintenance Arm (EAMA) system. Fusion Eng Des 2016;104:40-45.

[5] Hilton M R, Fleischauer P D. Applications of Solid Lubricant Films in Spacecraft. Surf Coat Tech 1992;55:435-441.

[6] Lince J R. Effective Application of Solid Lubricants in Spacecraft Mechanisms. Lubricants 2020;8.

[7] Stewart T B, Fleischauer P D. Chemistry of Sputtered Molybdenum-Disulfide Films. Inorg Chem 1982;21:2426-2431.

[8] Prasad S V, Zabinski J S, Mcdevitt N T. Friction Behavior of Pulsed-Laser Deposited Tungsten Disulfide Films. Tribol T 1995;38:57-62.

[9] Donnet C, Martin J M, LeMogne T, Belin M. Super-low friction of MoS_2 coatings in various environments. Tribol Int 1996;29:123-128.

[10] Ross S, Sussman A. Surface Oxidation of Molybdenum Disulfide. J Phys Chem-Us 1955;59:889-892.

[11] Dudder G J, Zhao X Y, Krick B, Sawyer W G, Perry S S. Environmental Effects on the Tribology and Microstructure of MoS_2-Sb_2O_3-C Films. Tribol Lett 2011;42:203-213.

[12] Zeng C, Pu J B, Wang H X, Zheng S J, Chen R. Influence of microstructure on tribological properties and corrosion resistance of MoS_2/WS_2 films. Ceram Int 2020;46:13774-13783.

[13] Zhao X Y, Perry S S. The Role of Water in Modifying Friction within MoS_2 Sliding Interfaces. Acs Appl Mater Inter 2010;2:1444-1448.

[14] Bondarev A, Ponomarev I, Muydinov R, Polcar T. Friend or Foe? Revising the Role of Oxygen in the Tribological Performance of Solid Lubricant MoS_2. Acs Appl Mater Inter 2022;14:55051-55061.

[15] Li Z W, Wang D S, Ye Q L, He J, Sun J Y, Weng L J, Hu M, Gao X M. The effect of oxygen introduced by WO_3 on the structure and tribological performance of W-S-O sputtered films. Tribol Int 2024;193:109408.

[16] Sheehan P E, Lieber C M. Nanotribology and nanofabrication of MoO_3 structures by atomic force microscopy. Science 1996;272:1158-1161.

[17] Kamiya S, Tsuda D, Miura K, Sasaki N. MoS_2 (0001)/MoO_3 (010)/MoS_2 (0001) friction-reducing system. Wear 2004;257:1133-1136.

[18] Liang T, Sawyer W G, Perry S S, Sinnott S B, Phillpot S R. First-principles determination of static potential energy surfaces for atomic friction in MoS_2 and MoO_3. Phys Rev B 2008;77.

[19] Johnston R R, Moore A J W. Water Adsorption on Molybdenum Disulfide Containing Surface Contaminants. J Phys Chem-Us 1964;68:3399.

[20] Khare H S, Burris D L. The Effects of Environmental Water and Oxygen on the Temperature-Dependent Friction of Sputtered Molybdenum Disulfide. Tribol Lett 2013;52:485-493.

[21] Yang Z X, Bhowmick S, Sen F G, Alpas A T. Microscopic and atomistic mechanisms of sliding friction of MoS_2: Effects of undissociated and dissociated H_2O. Appl Surf Sci 2021;563:150270.

[22] Li S H, Liu K Y, Klimes J, Chen J. Understanding the wetting of transition metal dichalcogenides from an perspective. Phys Rev Res 2023;5.

[23] Bobbitt N S, Curry J F, Babuska T F, Chandross M. Water adsorption on MoS_2 under realistic atmosphere conditions and impacts on tribology. Rsc Adv 2024;14:4717-4729.

[24] Yang Z X, Zhang X K, Gao K X, Zhang B, Sen F G, Bhowmick S, Zhang J Y, Alpas A T. Temperature-Dependent Frictional Behavior of MoS_2 in Humid Environments: Insights from Water Molecule Adsorption and DFT Analyses. Acs Appl Mater Inter 2024;16:13267-13281.

[25] Huang Y Q, Gao H Y, Yu K H, Niu Z W, Yang Z X, Zhang B, Gao K X, Zhang J Y, Alpas A T. Friction mechanisms of WS_2 in humid environments: Investigating H_2O adsorption via DFT computations and sliding friction experiments. Tribol Int 2025;203:110416.

[26] Xu S S, Gao X M, Hu M, Sun J Y, Jiang D, Zhou F, Liu W M, Weng L J. Nanostructured WS_2-Ni composite films for improved oxidation, resistance and tribological performance. Appl Surf Sci 2014;288:15-25.

[27] Wang M, Ma L Q, Chen H, Zhou S G, Lu Z B, Hou C J. First-principles calculations to explore the oxygen effects on WS_2 film in marine environments. Appl Surf Sci 2021;566:150741.

[28] Yang J, Wang D S, Fu Y L, Wang Q Q, Hu M, Jiang D, Gao X M, Sun J Y, Weng L J. Improving the tribological and anti-corrosion property of the WS_2 film through Ta doping. Vacuum 2021;192:110485.

[29] Series P, Nicholson E, Tarn J, Barri N, Chemin J B, Wang G R, Michel Y, Singh C V, Choquet P, Saulot A, Filleter T, Colas G. High Performance Space Lubrication of MoS_2 with Tantalum. Adv Funct Mater 2022;32:2110429.

[30] Sun L, Yang Z X, Zhang B, Xing Z Y, Zhang J Y, Wang F G, Qiang L. Superlubricity via operando formation of MoS_2/S_8 heterojunctions on steel surface with amorphous carbon protection. Nano Energy 2024;123.

[31] Kubart T, Polcar T, Kopecky L, Novák R, Nováková D. Temperature dependence of tribological properties of MoS_2 and $MoSe_2$ coatings. Surf Coat Tech 2005;193:230-233.

[32] Domínguez-Meister S, Rojas T C, Brizuela M, Sánchez-López J C. Solid lubricant behavior of MoS_2 and WSe_2-based nanocomposite coatings. Sci Technol Adv Mat 2017;18:122-133.

[33] Bin Yaqub T, Nadeem I, Fernandes F, Yaqoob K, Kalin M, Cavaleiro A. Nitrogen alloyed $MoSe_2$ coatings - Role of optimized morphology, structure and mechanical properties on diverse environment sliding performance. Tribol Int 2025;209.

[34] Polcar T, Evaristo M, Stueber M, Cavaleiro A. Mechanical and tribological properties of sputtered Mo-Se-C coatings. Wear 2009;266:393-397.

[35] Hudec T, Izai V, Satrapinskyy L, Huminiuc T, Roch T, Gregor M, Grancic B, Mikula M, Polcar T. Structure, mechanical and tribological properties of $MoSe_2$ and Mo-Se-N solid lubricant coatings. Surf Coat Tech 2021;405.

[36] Bondarev A V, Kiryukhantsev-Korneev P V, Sheveyko A N, Shtansky D V. Structure, tribological and electrochemical properties of low friction TiAlSiCN/MoSeC coatings. Appl Surf Sci 2015;327:253-261.

[37] Vuchkov T, Bin Yaqub T, Evaristo M, Cavaleiro A. Synthesis, microstructural and mechanical properties of self-lubricating Mo-Se-C coatings deposited by closed-field unbalanced magnetron sputtering. Surf Coat Tech 2020;394.

[38] Chakrapani V. Correlative trends between tribological and electronic properties of dry lubricants: Influence of humidity and dopants. Tribol Int 2023;177.

[39] Yaqub T B, Nadeem I, Haq M A, Yasir M, Cavaleiro A, Kalin M. Investigating the Effects of Long-Term Ambient Air Storage on the Sliding Properties of N-Alloyed $MoSe_2$ Coatings. Nanomaterials-Basel 2025;15.

[40] Vazirisereshk M R, Hasz K, Zhao M Q, Johnson A T C, Carpick R W, Martini A. Nanoscale Friction Behavior of Transition-Metal Dichalcogenides: Role of the Chalcogenide. Acs Nano 2020;14:16013-16021.

[41] Shi J, Zhao R, Yang Z, Yang J, Zhang W, Wang C, Zhang J. Template-free scalable growth of vertically-aligned MoS_2 nanowire array meta-structural films towards robust superlubricity. Materials Horizons 2023;10:4148-4162.

[42] Wang D S, Li Z W, Guo L B, Ye Q L, He J, Liu Z L, Jiang D, Fu Y L, Gao X M, Sun J Y, Weng L J, Hu M. Improved tribological properties of W-S-C-N film contributed by the friction-induced well crystallized thick transfer layer. Tribol Int 2024;198:109922.

[43] Wang Q, Tu J P, Zhang S C, Lai D M, Peng S M, Gu B. Effect of Ag content on microstructure and tribological performance of WS_2-Ag composite films. Surf Coat Tech 2006;201:1666-1670.

[44] Babuska T F, Mings A, Larson S R, Dugger M T, Rodriguez M A, Curry J F. Microstructural Assessment of Molybdenum Disulfide Coatings Using Nanoindentation Hardness. Acs Appl Mater Inter 2025;17:4210-4217.

[45] Kresse G, Furthmuller J. Efficiency of ab-initio total energy calculations for metals and semiconductors using a plane-wave basis set. Comp Mater Sci 1996;6:15-50.

[46] Perdew J P, Chevary J A, Vosko S H, Jackson K A, Pederson M R, Singh D J, Fiolhais C. Atoms, Molecules, Solids, and Surfaces - Applications of the Generalized Gradient Approximation for Exchange and Correlation. Phys Rev B 1992;46:6671-6687.

[47] Perdew J P, Burke K, Ernzerhof M. Generalized gradient approximation made simple. Phys Rev Lett 1996;77:3865-3868.

[48] Lee K, Murray É D, Kong L Z, Lundqvist B I, Langreth D C. Higher-accuracy van der Waals density functional. Phys Rev B 2010;82:081101.

[49] Hamada I. van der Waals density functional made accurate. Phys Rev B 2014;89:106-112.

[50] Berland K, Cooper V R, Lee K, Schröder E, Thonhauser T, Hyldgaard P, Lundqvist B I. van der Waals forces in density functional theory: a review of the vdW-DF method. Rep Prog Phys 2015;78:066501.

[51] Monkhorst H J, Pack J D. Special Points for Brillouin-Zone Integrations. Phys Rev B 1976;13:5188-5192.

[52] Zhou C J, Yang W H, Zhu H L. Mechanism of charge transfer and its impacts on Fermi-level pinning for gas molecules adsorbed on monolayer WS_2. J Chem Phys 2015;142:214704.

[53] He J G, Hummer K, Franchini C. Stacking effects on the electronic and optical properties of bilayer transition metal dichalcogenides MoS_2, $MoSe_2$, WS_2, and WSe_2. Phys Rev B 2014;89:075409.

[54] Zobeiri H, Xu S, Yue Y A, Zhang Q Y, Xie Y S, Wang X W. Effect of temperature on Raman intensity of nm-thick WS_2 : combined effects of resonance Raman, optical properties, and interface optical interference. Nanoscale 2020;12:6064-6078.

[55] Zhou P S, Schiettecatte P, Vandichel M, Rousaki A, Vandenabeele P, Hens Z, Singh S. Synthesis of Colloidal WSe_2 Nanocrystals: Polymorphism Control by Precursor-Ligand Chemistry. Cryst Growth Des 2021;21:1451-1460.

[56] Moser J, Levy F. Crystal Reorientation and Wear Mechanisms in MoS_2 Lubricating Thin-Films Investigated by Tem. J Mater Res 1993;8:206-213.